Multi-octave mid-infrared supercontinuum and frequency comb generation in a suspended As_2Se_3 ridge waveguide

ZELI LI,[1] JINHUI YUAN,[1,2,3*] CHAO MEI,[1] FENG LI,[3] XIAN ZHOU,[2,3] BINBIN YAN,[1] QIANG WU,[4] KUIRU WANG,[1] XINZHU SANG,[1] KEPING LONG,[2] AND CHONGXIU YU[1]

[1]*State Key Laboratory of Information Photonics and Optical Communications, Beijing University of Posts and Telecommunications (BUPT), Beijing 100876, P. R. China.*
[2]*Research Center for Convergence Networks and Ubiquitous Services, University of Science & Technology Beijing (USTB), Beijing 100083, P. R. China.*
[3]*Photonics Research Centre, Department of Electronic and Information Engineering, The Hong Kong Polytechnic University, Hung Hom, Hong Kong.*
[4]*Department of Physics and Electrical Engineering, Northumbria University, Newcastle upon Tyne, NE1 8ST, United Kingdom.*
*Corresponding author: yuanjinhui81@bupt.edu.cn

Received XX Month XXXX; revised XX Month, XXXX; accepted XX Month XXXX; posted XX Month XXXX (Doc. ID XXXXX); published XX Month XXXX

In this paper, we numerically investigate the mid-infrared supercontinuum (SC) generation in a suspended As_2Se_3 ridge waveguide, which is designed with the two zero-dispersion wavelengths. Simulation results show that when the pump pulses at wavelength 3.3 μm with width of 100 fs and peak power of 900 W are launched into the anomalous dispersion region of the designed waveguide with a length of 0.87 mm, the SC can be generated in the wavelength range from 1.76 to 14.42 μm (more than 3 octaves), extending deep into the "fingerprint" region. The stability of the generated SC is confirmed by the first-order coherence. Moreover, we demonstrate the performance of the SC-based frequency comb by assuming a 50-pulses pump source at a repetition rate of 100 MHz. © 2019 Optical Society of America

***OCIS codes*:** (320.6629) Supercontinuum generation; (190.4390) Nonlinear optics, integrated optics; (130.0250) Optoelectronics.

http://dx.doi.org/10.1364/AO.99.099999

1. INTRODUCTION

Mid-infrared (MIR) supercontinuum (SC) generation has attracted increasing research interests because of its significant applications in different fields, such as spectroscopy, frequency metrology, and biochemical sensing etc. [1-5]. The SC generation is a result of various nonlinear optical effects including self-phase modulation (SPM), cross-phase modulation (XPM), four-wave mixing (FWM), stimulated Raman scattering (SRS), soliton dynamics (SD), and dispersive wave (DW) [6-8]. Many works are concentrated on the SC generation in the waveguides, fibers or photonic crystal fibers (PCFs) fabricated from the silica or silicon materials [9-14]. However, the relatively weak nonlinearity of the silica material requires the pump source to have high peak power for the SC generation. In addition, the high absorption loss of the silica material beyond 2.4 μm imposes the limitation on the spectral broadening into the MIR region. And the transparency window of silicon in the MIR region ranges from 2.2 to 8.5 μm. By comparison, the chalcogenide glasses (ChGs) have unique advantages. The ChGs consist of chalcogen elements (S, Se, and Te), mixing with other elements such as As, Ge, P, and Sb [15]. They have a wide MIR transparency window and show high Kerr nonlinearity as well as low two-photon absorption (TPA) [16]. Therefore, they are considered as excellent candidates for the MIR SC generation [17].

Recently, the MIR SC generations in the ChGs have drawn lots of attentions [18-23]. The chalcogenide optical fibers have been extensively studied to generate the octave-spanning SCs in the MIR regions [24-27]. However, the pump pulses with peak power of tens of kilowatts are required to generate the octave-spanning SC by using chalcogenide optical fibers, and the optical fiber structure and experimental system stability could be damaged by the high peak power. In contrast, the broadband MIR SC, extending deeply into the "fingerprint" region, can be generated in chalcogenide waveguides when the pump pulses with low peak power are used. In 2012, Gai et al. designed a dispersion-engineered As_2S_3 rib waveguide for the MIR SC generation spanning from 2.9 to 4.2 μm [28]. In 2015, Karim et al. reported the MIR SC generation from 1.8 to 7.7 μm (more than 2 octaves) in $Ge_{11.5}As_{24}Se_{64.5}$ channel waveguide [29]. In 2017, Saini et al preliminarily demonstrated the MIR SC generation in an all-normal dispersion As_2Se_3 rib waveguide, where nonlinear process is dominated by the SPM and optical wave breaking [30]. In 2018, Karim et al numerically demonstrated the MIR SC generation in an As_2Se_3 channel waveguide which exhibited nearly flat anomalous dispersion.

When the pump source at 6 μm with the pulse duration of 170-fs is used, an ultrabroadband SC covering the wavelength from 3.5 to 15 μm is shown with the largest input peak power of 10 kW [31]. When the pump pulses operate in the anomalous dispersion region, the SD and DW effects can easily happen, which is beneficial to the multi-octave MIR SC generation.

In this paper, we report the multi-octave MIR SC generation in a suspended As_2Se_3 ridge waveguide designed with the two zero-dispersion wavelengths (ZDWs) when pump pulses work in the anomalous dispersion region. The influences of the pump pulse parameters including the wavelength, pulse width, and peak power on the MIR SC generation are investigated. Moreover, the nonlinear dynamics for different waveguide lengths are also analyzed. Finally, the SC-based frequency comb generation is demonstrated.

2. THEORETICAL MODEL

To investigate the evolution of the short pulses in the proposed waveguide, the generalized nonlinear Schrödinger equation (GNLSE) [32] is introduced as following

$$\frac{\partial A}{\partial z}+\frac{\alpha A}{2}+i\sum_{m=2}^{\infty}\beta_n\frac{(-i)^m\beta_m}{m!}\frac{\partial^m A}{\partial t^m}=i\sum_{n=0}^{\infty}\frac{\gamma_n i^n}{n!}\frac{\partial^n}{\partial t^n}\times\left[A(z,t)\int_0^{\infty}R(t')\left|A(z,t-t')\right|^2dt'\right], \quad (1)$$

where $A(z, t)$ is defined as the slowly-varying envelope of the electric field. α represents the linear loss, β_m (m=2, 3, 4, 5, ..., and 12) is the m-order dispersion coefficient, which is associated with the Taylor expansion of the propagation constant $\beta(\omega)$ at the carrier frequency ω. In the simulation, a constant material loss coefcient of 6.5×10^{-4} dB/mm is considered for the entire range of the optical spectrum [33]. The effective mode field area A_{eff} is included in the calculation of nonlinear coefficient γ_0, which is defined as $\gamma_0 = 2\pi n_2/\lambda A_{eff}$, where $n_2 = 2.4\times10^{-17}$ m^2/w is the nonlinear refractive index for the As_2Se_3 material [34-36], and λ is the pump wavelength. The nth-order coefficient γ_n is defined as $\gamma_n = \omega_0\,\partial^n[\gamma(\omega)/\omega]/\partial\omega^n$, where ω_0 is the angular frequency of the pulse.

The wavelength-dependent linear refractive indices of MgF_2 and As_2Se_3 glasses are calculated using the Sellmeier equations given in Refs. [37] and [38] respectively.

The nonlinear response function $R(t')$ takes into account of the electronic and nuclear contributions and can be expressed as

$$R(t')=(1-f_R)\delta(t')+f_R h_R(t'), \quad (2)$$

where f_R = 0.115 represents for the fractional contribution of the Raman response, and $h_R(t')$ is the delayed Raman response function described as

$$h_R(t')=\frac{\tau_1^2+\tau_2^2}{\tau_1\tau_2^2}\exp\left(-\frac{t'}{\tau_2}\right)\sin\left(\frac{t'}{\tau_1}\right), \quad (3)$$

where, τ_1 = 23.1 fs is the phonon oscillation frequency and τ_2 = 195 fs is the characteristic damping time of atoms vibration, respectively [39].

To investigate the spectral coherence of the generated SC, the first-order coherent is calculated with the random noise as

$$g_{12}^{(1)}(\lambda,t_1-t_2)=\left|\frac{\langle A_1^*(\lambda,t_1)\,A_2(\lambda,t_2)\rangle}{\sqrt{\langle|A_1(\lambda,t_1)|^2\rangle\langle|A_2(\lambda,t_2)|^2\rangle}}\right|, \quad (4)$$

where $A(\lambda, t)$ is the amplitude of the SC generated with the random noise seeds, λ is the pump wavelength, and t_1 and t_2 are the time delays between the pulses. The angular brackets represent an ensemble average over independently pairs of spectra, i.e. $A_1(\lambda, t)$ and $A_2(\lambda, t)$, which are obtained from 50 shot-to-shot simulations with different random noises at wavelength λ.

3. WAVEGUIDE DESIGN AND CHARACTERISTICS

The cross-section of the designed suspended As_2Se_3 ridge waveguide is shown in Fig. 1(a). The As_2Se_3 layer is suspended above the MgF_2 substrate with a thick air gap. The top of As_2Se_3 layer is over-etched to form the ridge structure. Such a waveguide structure is beneficial to confine the propagation light field into the As_2Se_3 layer even at wavelength 12 μm. Meanwhile, since the As_2Se_3 channel is covered by the air, the designed waveguide has a much larger refractive index contrast, which results in a stronger mode field confinement. The waveguide coupling can be achieved by a tapered fiber, and the coupling losses for the quasi-TE mode and quasi-TM mode are less than 1 dB. The width and height of the ridge are W and H_1, respectively, and the height of the slab layer is H_2. The suspended structure can be formed by selectively removing the buried fluoride. Traditional optical lithography with plasma reactive-ion dry etching may be used to form the air gap. In order to provide enough space between the As_2Se_3 and MgF_2 layers, the thickness of the air gap is chosen as 2 μm.

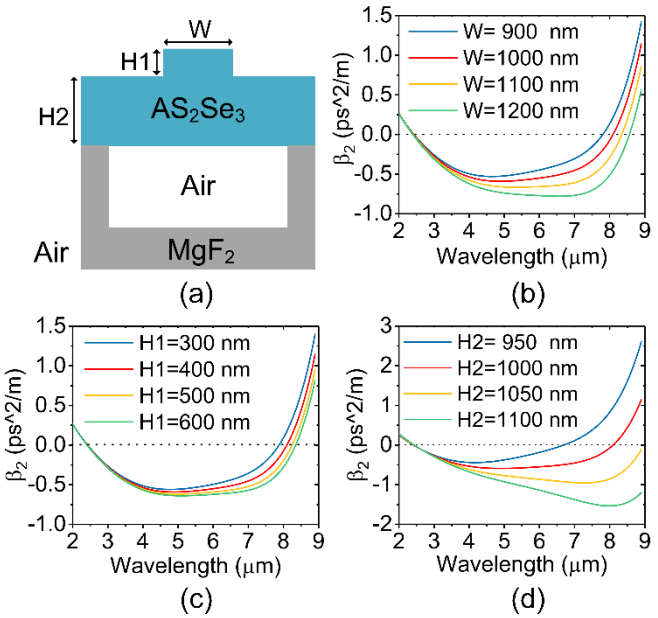

Fig. 1. (a) The cross-section of the designed suspended As_2Se_3 ridge waveguide. The GVD coefficients of the quasi-TE mode as functions of wavelength when (b) W, (c) H_1, and (d) H_2 is varied, respectively.

The dispersion can be controlled by tailoring the geometrical parameters of the waveguide. The full-vector finite element method is used to investigate the dispersion characteristics of the waveguide with different geometrical parameters. Figs. 1(b), 1(c), and 1(d) show the calculated GVD coefficients of the quasi-TE mode when W, H_1, and H_2 is varied, respectively. For different W, H_1, and H_2, it is noted that all

waveguides have the two ZDWs with the flat and low anomalous dispersion. Besides, the GVD is very sensitive to both W and H_2. The second ZDW can be red-shifted by increasing W, H_1, or H_2, but the first ZDW is red-shifted slightly when only H_2 is increased. As shown in Fig. 1(b), if W is increased while H_1 and H_2 remain unchanged, the anomalous dispersion region gradually increases. In Fig. 1(c), the GVD changes very little with H_1. In Fig. 1(d), the GVD peak is red-shifted and the value increases with the increasing H_2. To make SC extend deeply into the "fingerprint" region, the pump wavelength should be located at a longer wavelength but close to the first ZDW. This can be realized by carefully selecting H_2. In addition, the GVD value in the anomalous dispersion region increases when W, H_1, or H_2 increases. However, the increment of H_2 is not beneficial to the spectral broadening because A_{eff} is increased and the nonlinear interaction becomes weak.

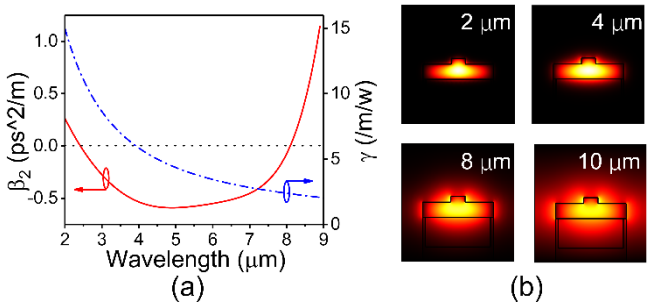

Fig. 2. (a) The calculated GVD and nonlinear coefficient γ as functions of wavelength, and (b) the mode field distributions of quasi-TE mode calculated at wavelengths 2, 4, 8, and 10 μm, respectively.

According to the above analysis, the geometrical parameters of the designed waveguide are chosen as W=1.0 μm, H_1=0.4 μm, and H_2=1.0 μm, respectively. Fig. 2(a) shows the calculated β_2 as a function of wavelength for the quasi-TE mode. The wavelength dependences of the As_2Se_3 and MgF_2 materials are considered in the determination of dispersion characteristic. The two ZDWs are located at 2.43 and 8.12 μm, respectively, along with an anomalous dispersion region of 5.69 μm. Moreover, the relationship between γ and wavelength is also shown in Fig. 2(a). It can be seen from Fig. 2(a) that the variation of γ is monotonic. Fig. 2(b) shows the mode field distributions of the quasi-TE mode, which indicates the polarization of the electric field in the x direction. And the electric field distribution is used to represent the distribution of energy. Fig. 2(b) shows the mode field distributions of quasi-TE mode calculated at wavelengths 2, 4, 8, and 10 μm, respectively. From Fig. 2(b), the mode fields are well confined in the slab even at wavelength 10 μm.

4. SIMULATION RESULTS AND DISCUSSION

In the simulation, the pump pulse is operated at the anomalous dispersion region of the waveguide, where the MIR SC generation is mainly resulted from the combined SD and DW effects. In the following, we will investigate the influences of the pump pulse parameters and waveguide length on the MIR SC generation.

When the wavelength of the pump pulse with the peak power of 900 W and width of 100 fs is changed from 2.7 to 3.6 μm, the temporal and spectral profiles in after a propagation of 0.87 mm are shown in Figs. 3(a) and 3(b), respectively. From Fig. 3(a), some small peaks can be observed and the solitons move toward the original position in the time domain. From Fig. 3(b), the optical spectrum is gradually broadened when the pump wavelength is changed from 2.7 to 3.3 μm. Especially for the pump wavelength 3.3 μm, the optical spectrum width reaches its maximum. The -40 dB bandwidth of the SC generated spans from 1.76 to 14.42 μm (more than 3 octaves), extending deep into the "fingerprint" region. The physical mechanism on the MIR SC generation is as following. Because the pump wavelength is located at the anomalous dispersion region of the waveguide, the SD including the soliton self-frequency shift (SSFS) and soliton fission (SF) dominates the nonlinear optical process. In the process of the SSFS and SF, when the resonance matching conditions involving the higher-order dispersion are satisfied, the blue- and red-shifted DWs are generated at the shorter and longer wavelength sides due to the positive and negative dispersion slopes of β_2 curve with the two ZDWs. After that, the XPM which occurs between the solitons and the DWs will also further broaden the optical spectrum. However, when the pump wavelength is located at 3.6 μm, the optical spectrum stops broadening and becomes narrower. The main reason is considered as following. First, for the longer pump wavelength, the anomalous dispersion range which the SSFS and SF are experiencing is smaller. Second, the SSFS process will be more remarkable suppressed by the second ZDW. Therefore, it is important to appropriately choose the pump wavelength for the multi-octave MIR SC generation.

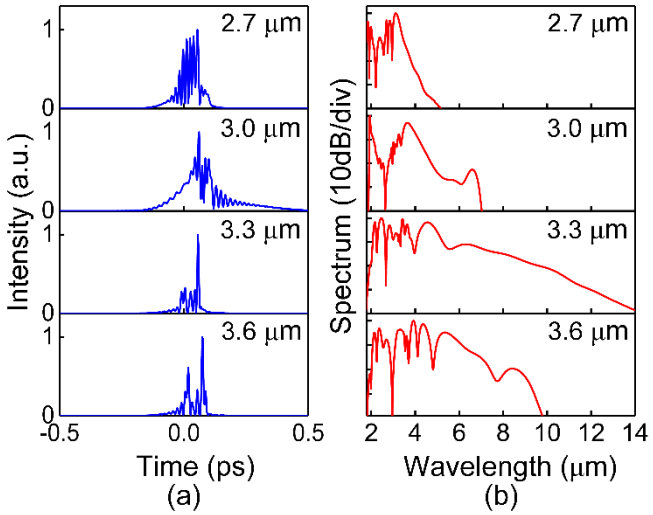

Fig. 3. (a) Temporal and (b) spectral profiles of the SC when the pump pulse wavelength is located at 2.7, 3.0, 3.3, and 3.6 μm, respectively.

When the pump pulse at 3.3 μm with the widths of 100, 150, 200, and 250 fs is launched into a 0.87-mm long waveguide, the temporal and spectral profiles are shown in Figs. 4(a) and 4(b), respectively. It should be noted that the micron-scale length is not difficult to achieve by using the current waveguide fabrication technique. As the pulse width is increased from 100 to 250 fs, the soliton order, which is related to the pulse width and peak power [8,40], is calculated as 11.2, 16.8, 22.5, and 28.1, respectively. When the pump pulse width is chosen as 100 fs, the soliton separation distance is 0.76 mm. At this time, the soliton fission occurs evidently, and the number of the small peaks increases and the solitons move toward the right side of the original position in the time domain. The corresponding optical spectrum is greatly broadened. When the pump pulse width is chosen as 150, 200, and 250 fs, the soliton separation distance is 1.13,1.51, and 1.89 mm, respectively. At this time, the apparent soliton fission cannot be observed because of the shorter waveguide length. The optical spectrum has multi-peaks and the spectral bandwidth at -40 dB becomes narrower. Therefore, the pump pulse with width of 100 fs is more favorable for the generation of multi-octaves MIR SC in the designed waveguide.

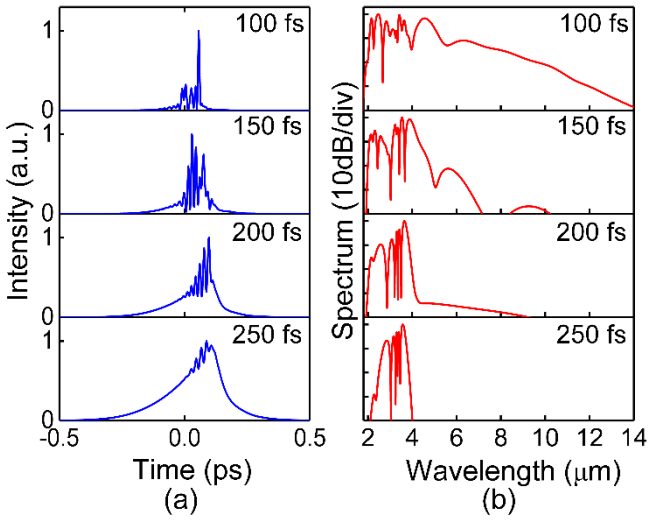

Fig. 4. (a) Temporal and (b) spectral profiles of the SC generated when the pump pulse width is chosen as 100, 150, 200, and 250 fs, respectively.

In the following, we will investigate the influence of the pump peak power on the MIR SC generation. Figs. 5(a) and 5(b) show the temporal and spectral profiles when the peak power of the pump pulse at 3.3 μm with the width of 100 fs is changed from 300 to 900 W. The soliton order is calculated as 6.5, 8.4, 9.9, and 11.2 as the peak power is increased from 300, to 500, to 700, and to 900 W, respectively. From Fig. 5(a), the satellites become larger and the solitons move toward the original position at the same time as the peak power increases. From Fig. 5(b), the corresponding bandwidth of the optical spectrum is increased since the nonlinear effects can be enhanced by the higher peak power. When the peak power is increased up to 900 W, the MIR SC generated can be more than three octaves.

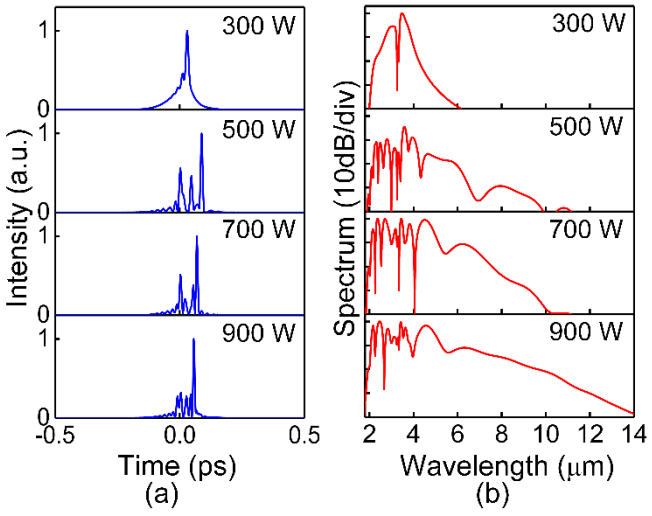

Fig. 5. (a) Temporal and (b) spectral profiles of the SC generated when the pump peak power is chosen as 300, 500, 700, and 900 W, respectively.

We will demonstrate the nonlinear dynamics of the MIR SC generation for different waveguide lengths. When the width and peak power of the pump pulse at 3.3 μm are chosen as 100 fs and 900W, the temporal and spectral profiles for the waveguide lengths of 0, 0.61, 0.87, and 1 mm are shown in Figs. 6(a) and 6(b), respectively. From Fig. 6 (a), many small peaks emerge and the solitons move toward the right side of the original position in the time domain as the waveguide length increases. From Fig. 6(b), when the waveguide length is increased from 0 to 0.87 mm, the spectral bandwidth is also increased. Especially for the waveguide length of 0.87 mm, the spectral range spans from 1.76 to 14.42 μm. However, when the waveguide length is increased up to 1 mm, the optical spectrum does not continue to widen. Figs. 6 (c) and 6(d) show the corresponding temporal and spectral evolutions. From Figs. 6(c) and (d), the SPM causes the obvious spectral broadening at the beginning stage. As the waveguide length increases, the temporal pulse is significantly compressed due to the relatively low and flat dispersion. But the propagation loss restricts the extension of the optical spectrum for the longer waveguide length.

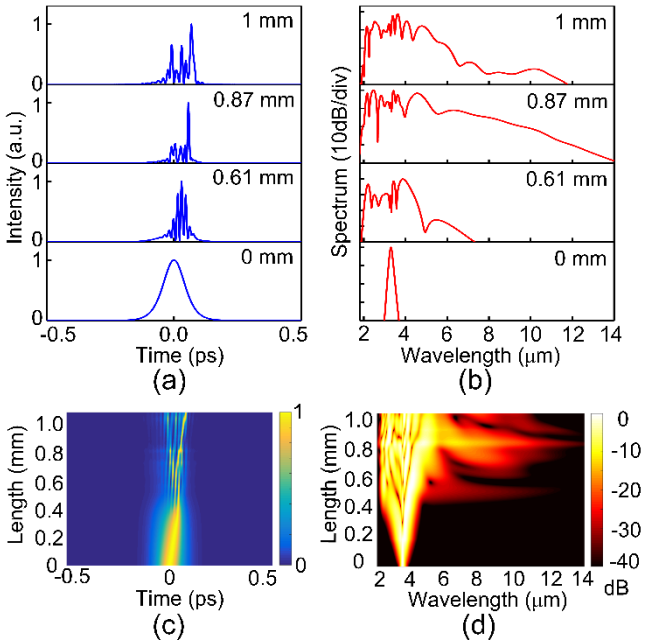

Fig. 6. (a) Temporal and (b) spectral profiles of the SC generated when the waveguide length is 0, 0.61, 0.87, and 1 mm, respectively. The evolution of (c) temporal and (d) spectral profiles in the designed waveguide when the pump pulse with width of 100 fs and peak power of 900 W is used.

The degree of coherence $g_{12}^{(1)}$ is calculated to confirm the stability of the generated MIR SC. The pump peak power and propagation length are chosen as 900 W and 0.87 mm, respectively. For the SC generated with the picosecond pulse, the unavoidable intrinsic noise degrades the coherence of the SC. To investigate the effect of the noise, the following optical pulse with shot noise is injected into the designed waveguide

$$A(t) = P_0^{1/2} \operatorname{sech}\left(\frac{t}{T_0}\right)\left[\exp\left(\frac{i\xi t^2}{2}\right) + \eta \hat{N} \exp\left(i2\pi \hat{U}\right)\right], \quad (5)$$

where $\hat{N}$ is a normally distributed random variable with mean value of 0 and standard deviation of 1, and $\hat{U}$ is a uniformly distributed random variable between 0 and 1. The noise factor η indicates the amplitude of the noise relative to the pulse amplitude. In the simulation, $\eta = 1\times10^{-2}$ and $\eta = 1\times10^{-4}$ are used, respectively. A pulse train including 50 pulses with a repetition rate of 100 MHz is launched into

the waveguide for generating the SC-based frequency comb. The pump pulse train has periodicity in the time domain. According to the theory of Fourier transform, the spectrum of pulse train in the frequency domain is discrete. Due to the influence of the nonlinear and dispersive effects, the output pulse is compressed greatly in the time domain. In our simulation, the launched 50 pulses are the same except the imposed random noise.

Finally, we will analyze the influence of the random noise factor η on the MIR generation. Figs. 7(a), 7(b), 7(c), and 7(d) show the generated MIR SC and coherence calculated with the 50 shots for different η. The blue lines are the averaged spectrum of 50 shots, and the grey lines are the overlapped spectra of 50 shots with the random noise. When the pump pulse with the width of 100 fs and peak power of 900 W is launched into a 0.87-mm long waveguide, the overlapped and averaged spectra and coherence for $\eta = 1 \times 10^{-4}$ are shown in Figs. 7(a) and 7(c), respectively. It can be seen from Figs. 7(a) and 7(c) that the spectral fluctuation is very slight and the corresponding $g_{12}^{(1)}$ is close to 1 within the considered wavelength range. In contrast, under the same pump condition and waveguide length, the overlapped and averaged spectra and coherence for $\eta = 1 \times 10^{-2}$ are shown in Figs. 7(b) and 7(d), respectively. From Figs. 7(b) and 7(d), the spectral fluctuation becomes very evident and $g_{12}^{(1)}$ is seriously degraded.

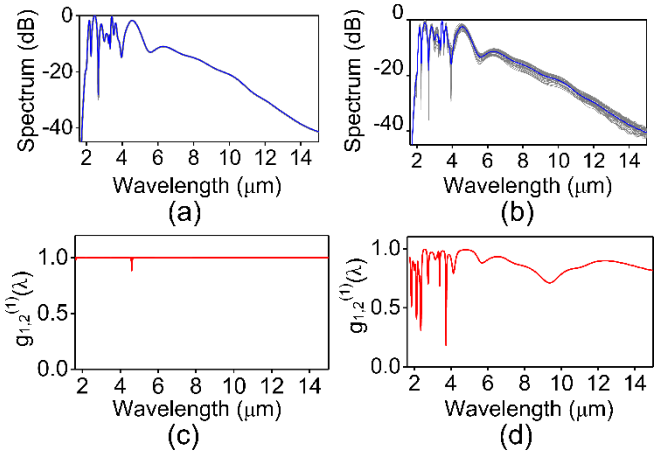

Fig. 7. (a) The spectra and (c) degree of coherence of the SC generated with $\eta = 1 \times 10^{-4}$. (b) The spectra and (d) degree of coherence of the SC generated with $\eta = 1 \times 10^{-2}$. The grey and blue lines in (a) and (b) represent the overlapped spectra of the 50 shots and average values of the 50 shots, respectively.

In order to generate the SC-based frequency comb, a pulse train included 50 pulses with a repetition frequency of 100 MHz is launched into the waveguide. The pump pulse train with the width of 100 fs and peak power of 900 W is used. Fig. 7(a) shows the SC-based frequency comb structure. Fig. 7(b) clearly shows the zoom-in view of the frequency comb generated at 90.85 THz/3.3 μm with a sampling bandwidth of 500 MHz. The comb line structure can be clearly seen from the zoom-in view with a frequency interval of 100 MHz.

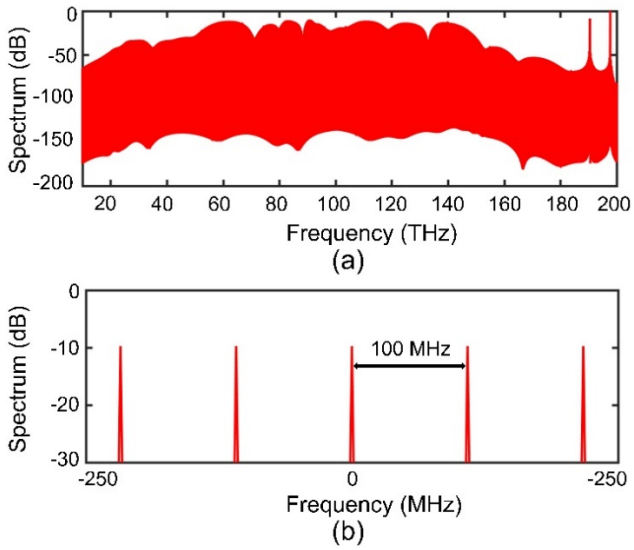

Fig. 8. (a) The SC-based frequency comb generated with 50 input pulses at the repetition rate of 100 MHz. (b) The corresponding zoom-in view of the frequency comb at 90.85 THz with a sampling bandwidth of 500 MHz.

For the problem of practical fabrication, some previous works were concentrated on the integrated chalcogenide glass. One of the works reported that a 30-μm-radius and 450-nm-thick microdisk resonator pulley coupled to an 800-nm-wide channel bus waveguide [41]. In another work, attention was paid to the mask fabrication. The photo-mask has a measured line edge roughness on straight waveguides of 6 nm RMS for a spatial fluctuation wavelength range of 0.6 to 62 μm [42]. Figs. 9(a)–(e) show a possible fabrication process of the designed waveguide. Firstly, the As_2Se_3 layer is grown on a MgF_2 substrate by the atmospheric chemical vapor deposition (CVD) technology [43], and then invert carefully the formed die as shown in Fig. 9(a). Secondly, we can form a suspended trench (Fig. 8(b)) by the traditional optical lithography with plasma reactive-ion dry etching [44,45]. Thirdly, the hydrophobic bonding techniques are used to make the etched die be directly bonded onto the MgF_2 wafer (Fig. 8(c)). The detailed bonding process is introduced in Ref. [46]. Finally, a metal mask is used to protect the ridge structure from etching, which is patterned by i-line lithography and lift-off [47]. The CF_4:O_2 plasma etching can be used to make sure the As_2Se_3 ridge layer is accomplished, and hydrofluoric acid dip is used to remove the metal mask (Fig. 8(d)).

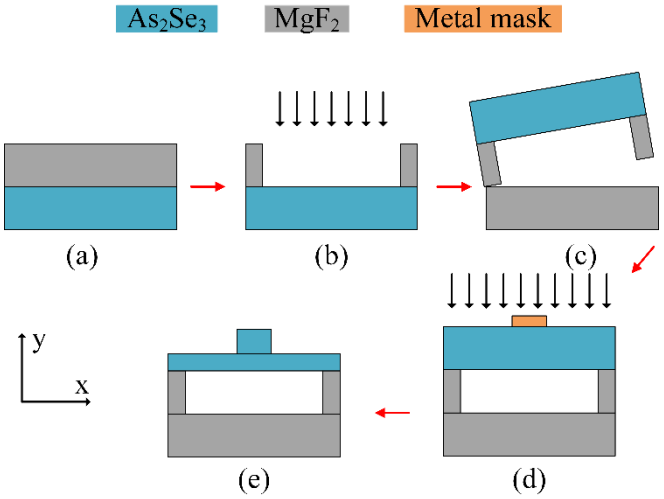

Fig. 9. A possible fabrication process flow: (a) deposition of As_2Se_3 on MgF_2 substrate and inversion, (b) formation of the suspended air trench, (c) MgF_2 hydrophobic bonding, (d) waveguide definition with metal mask and etching, and (e) final waveguide structure.

5. CONCLUSION

In summary, we design a suspended As_2Se_3 ridge waveguide with the two ZDWs. With the designed waveguide, we investigate the influences of the pump pulse parameters and waveguide length on the MIR SC generation. When the pump pulse at wavelength 3.3 μm with width of 100 fs and peak power of 900 W is launched into a 0.87-mm long waveguide, the MIR SC with the bandwidth of more than 3-octaves can be generated. Moreover, the performance of the SC-based frequency comb is demonstrated. It is believed that the proposed waveguide structure paves the way for obtaining the MIR SC source which would be highly desirable for the applications in the MIR photonics and spectroscopy.

Funding Information. This work was supported by National Natural Science Foundation of China (61875238), Beijing Youth Top-notch Talent Support Program (2015000026833ZK08), and the Fund of State Key Laboratory of Information Photonics and Optical Communications (BUPT) P. R. China (IPOC2017ZZ05).

References

1. F. K. Tittel, D. Richter, and A. Fried, "Mid-infrared laser applications in spectroscopy," in Handbook of Solid-State Mid-Infrared Laser Sources (Springer, 2003)
2. S. Haxha and H. Ademgil, "Novel design of photonic crystal fibers with low confinement losses, nearly zero ultraflattened chromatic dispersion, negative chromatic dispersion and improved effective mode area," Opt. Commun. **281**, 278–286 (2008).
3. I. Hartl, X. D. Li, C. Chudoba, R. K. Ghanta, T. H. Ko, J. G. Fujimoto, J. K. Ranka, and R. S. Windeler, "Ultrahigh-resolution optical coherence tomography using continuum generation in an air-silica microstructure optical fiber," Opt. Lett. **26**, 608–610 (2001).
4. A. Schliesser, N. Picque, and T. W. Hansch, "Mid-infrared frequency combs," Nat. Photonics 6, 440–449 (2012).
5. I. D. Aggarwal and J. S. Sanghera, "Development and application of chalcogenide glass optic fiber at NRL," J. Optoelectron. Adv. Mater. **4**, 665–678 (2002).
6. G. P. Agrawal, *Non-Linear Fiber Optics*, 5th ed. (Academic, 2013)
7. A. V. Husakou, J. Herrmann, "Supercontinuum Generation of Higher-Order Solitons by Fission in Photonic Crystal Fibers," Phys. Rev. lett. **87**, 203901- 203904 (2001).
8. J. M. Dudley, G. Genty, and S. Coen, "Supercontinuum generation in photonic crystal fiber," Rev. Mod. Phys. **78** ,1135-1184 (2006).
9. D. Y. Oh, D. Sell, H. Lee, K. Y. Yang, S. A. Diddams, and K. J. Vahala, "Supercontinuum generation in an on-chip silica waveguide," Opt. Lett. 39, 1046–1048 (2014).
10. K. Tarnowski, T. Martynkien, P. Mergo, J. Sotor, and G. Soboń, "Compact all-fiber source of coherent linearly polarized octave-spanning supercontinuum based on normal dispersion silica fiber," Scientific reports 9, 1-8 (2019).
11. M. L. Ferhat, L. Cherbi, and I. Haddouche, "Supercontinuum generation in silica photonic crystal fiber at 1.3 μm and 1.65 μm wavelengths for optical coherence tomography," Optik 152, 106-115 (2018).
12. F. De Leonardis, B. Troia, R. Soref, and V. M. N Passaro, "Modelling of supercontinuum generation in the germanium-on-silicon waveguided platform," J. Lightw. Techonl. 33, 4437–4444 (2015).
13. L. Shen et al., "Four-wave mixing and octave-spanning supercontinuum generation in a small core hydrogenated amorphous silicon fiber pumped in the mid-infrared," Opt. Lett. 39, 5721–5724 (2014).
14. L. Yin, Q. Lin, and G. P. Agrawal, "Soliton fission and supercontinuum generation in silicon waveguides," Opt. Lett. 32, 391–393 (2007)
15. A. Zakery and S. R. Elliott, "Optical properties and applications of chalcogenide glasses: a review," J. Non-Cryst. Solids 330, 1–12 (2003).
16. J. M. Harbold, F. O. Ilday, F. W. Wise, J. S. Sanghera, V. Q. Nguyen, L. B. Shaw, and I. D. Aggarwal, "Highly nonlinear As-S-Se glasses for all-optical switching," Opt. Lett. **27**, 119–121 (2002).
17. B. J. Eggleton, K. Richardson, "Chalcogenide photonics," Nat. Photonics **5**, 141-148 (2011).
18. T. S. Saini, A. Kumar, and R. K. Sinha, "Broadband mid-infrared supercontinuum spectra spanning 2–15 μm using As_2Se_3 chalcogenide glass triangular-core graded-index photonic crystal fiber," J. Lightwave Technol. **33**, 3914–3920 (2015).
19. Y. Yu, B. Zhang, X. Gai, C. Zhai, S. Qi, W. Guo, Z. Yang, R. Wang, D. Y. Choi, S. Madden, and B. Luther-Davies, "1.8-10 μm mid-infrared supercontinuum generated in a step-index chalcogenide fiber using low peak pump power," Opt. Lett. **40**, 1081–1084 (2015).
20. G. N. Chaitanya, T. S. Saini, A. Kumar, and R. K. Sinha, "Ultra broadband mid-IR supercontinuum generation in $Ge_{11.5}As_{24}Se_{64.5}$ based chalcogenide graded-index photonic crystal fiber: design and analysis," Appl. Opt. **55**, 10138–10145 (2016).
21. C. R. Petersen, U. Møller, I. Kubat, and B. Zhou, "Mid-Infrared Supercontinuum Covering the 1.4–13.3 μm Molecular Fingerprint Region Using Ultra-High NA Chalcogenide Step-Index Fibre," Nat. Photonics **8**, 830-834 (2014).
22. S. Xie, F. Tani, J. C. Travers, P. Uebel, C. Caillaud , J.T roles, and P. S. J. Russell, "As2S3–silica double-nanospike waveguide for mid-infrared supercontinuum generation," Opt. Lett. **39**, 5216-5219 (2014).
23. S. Xie, N. Tolstik, J. C. Travers, E. Sorokin, C. Caillaud, J. Troles, and I. T. Sorokina, "Coherent octave-spanning mid-infrared supercontinuum generated in As_2S_3-silica double-nanospike waveguide pumped by femtosecond Cr: ZnS laser," Opt. Lett. **24**, 12406-12413 (2016).
24. H. Saghaei, M. Ebnali-Heidari , and M. K. Moravvej-Farshi, "Mid-infrared supercontinuum generation via As2Se3 chalcogenide photonic crystal fibers." Appl. Opt. **54**, 2072-2079 (2015).
25. J. Hu, C. R. Menyuk, L. B. Shaw, J. S. Sanghera, and I. D. Aggarwal, "Maximizing the bandwidth of supercontinuum generation in As_2Se_3 chalcogenide fibers," Opt. Express **18**, 6722–6739 (2010).
26. A. B. Khalifa, A. B. Salem, and R. Cherif, "Mid-infrared supercontinuum generation in multimode As_2Se_3 chalcogenide photonic crystal fiber," Appl. Opt. **56**, 4319–4324 (2017).

27. R. Cherif and M. Zghal, "Ultrabroadband, midinfrared supercontinuum generation in dispersion engineered As_2Se_3-based chalcogenide photonic crystal fibers," Int. J. Opt. **2013**, 876474 (2013).
28. X. Gai, D.-Y. Choi, S. Madden, Z. Yang, R. Wang, and B. Luther-Davies, "Supercontinuum generation in the mid-infrared from a dispersion - engineered As_2S_3 glass rib waveguide," Opt. Lett. **37**, 3870–3872 (2012).
29. M. R. Karim, B. M. Rahman, and G. P. Agrawal, "Mid-infrared supercontinuum generation using dispersion-engineered $Ge_{11.5}As_{24}Se_{64.5}$ chalcogenide channel waveguide," Opt. Express **23**, 6903-6914 (2015).
30. T. S. Saini, A. Kumar, and R. K. Sinha, "Design and modeling of dispersion engineered rib waveguide for ultra-broadband mid-infrared supercontinuum generation," J. Mod. Opt. **64**, 143–149 (2017).
31. M. R. Karim, H. Ahmad, S. Ghosh, and B.M.A. Rahman, "Design of dispersion-engineered As_2Se_3 channel waveguide for mid-infrared region supercontinuum generation," J. Appl. Phys. **123**, 213101 (2018).
32. M. Yang, Y. Guo, J. Wang, Z. Han, K. Wada, L. C. Kimerling, A. M. Agarwal, J. Michel, G. Li, and L. zhang, "Mid-IR supercontinuum generated in low dispersion Ge-on-Si waveguides pumped by sub-ps pulses," Opt. Express **25**, 16116-16122 (2017).
33. V. S. Shiryaev, and M. F. Churbanov, "Trends and prospects for development of chalcogenide fibers for mid-infrared transmission," J. Non-Crys. Solids **377**,225-230 (2013).
34. B. Ung and M. Skorobogatiy, "Chalcogenide microporous fibers for linear and nonlinear applications in the mid-infrared," Opt. Express **18**, 8647–8659 (2010).
35. R. E. Slusher, G. Lenz, J. Hodelin, J. Sanghera, L. B. Shaw, and I. D. Aggarwal, "Large Raman gain and nonlinear phase shifts in high-purity As_2Se_3 chalcogenide fibers," J. Opt. Soc. Am. B **21**, 1146–1155 (2004).
36. T. S. Saini, U. K. Tiwari, and R. K. Sinha, "Design and analysis of dispersion engineered rib waveguides for on-chip mid-infrared supercontinuum," J. Lightw. Technol. **36**, 1993-1999 (2018).
37. M. J. Dodge, "Refractive Properties of Magnesium Fluoride," Appl. Opt. **23**, 1980–1985 (1984).
38. H. G. Dantanarayana, N. Abdel-Moneim, Z. Tang, L. Sojka, S. Sujecki, D. Furniss, A. B. Seddon, I. Kubat, O. Bang,and T. M. Benson, "Refractive index dispersion of chalcogenide glasses for ultra-high numerical-aperture fiber for mid-infrared supercontinuum generation," Opt. Mater. Express **4**,1444–1455 (2014).
39. B. Ung, and M. Skorobogatiy, "Chalcogenide microporous fibers for linear and nonlinear applications in the mid-infrared," Opt. Express 18, 8647–8659 (2010).
40. F. Xu, J. H. Yuan, C. Mei, F. Li, Z. Kang, B. B. Yan, X. Zhou, Q. Wu, K. R. Wang, X. Z. Sang, C. X. Yu, and G. Farrell, "Mid-infrared selfsimilar pulse compression in a tapered tellurite photonic crystal fiber and its application in supercontinuum generation," J. Lightwave Technol. **36**, 3514–3521 (2018).
41. L. Li, H. Lin, S. Qiao, Y. Zou, S. Danto and K. Richardson, et al. "Integrated flexible chalcogenide glass photonic devices," Nat. Photonics 8, 643-649(2014).
42. S. J. Madden, D. Y. Choi, D. A. Bulla, A. V.Rode, B. Luther-Davies, V. G. Ta'eed, M. D. Pelusi, and B. J. Eggleton, "Long, low loss etched As2S3 chalcogenide waveguides for all-optical signal regeneration," Opt. Express 15, 14414-14421 (2007).
43. R. Loo, G. Wanga, L. Souriaua, J. C. Linc, S. Takeuchia, G. Brammertza and M. Caymaxa, "High quality Ge virtual substrates on Si wafers with standard STI patterning," J. Electrochem. Soc. 157, H13–H21(2010).
44. K. Suzuki, Y. Hamachi, and T. Baba, "Fabrication and characterization of chalcogenide glass photonic crystal waveguides," Opt. Express 17, 22393-22400 (2009).
45. Y. Ruan, W. Li, R. Jarvis, N. Madsen, A. Rode, and B. Luther-Davies, "Fabrication and characterization of low loss rib chalcogenide waveguides made by dry etching," Opt. Express 12, 5140–5145 (2004).
46. J. Chiles, S. Khan, J. C. Ma, and S. Fathpour, "High-contrast, all-silicon waveguiding platform for ultra-broadband mid-infrared photonics," Appl. Phys. Lett. 103, 151106 (2013).
47. A. Malik. S. Dwivedi, L. V. Landschoot, M. Muneeb, Y. Shimura, G. Lepage, J. V. Campenhout, W. Vanherle, T. V. Opstal, R. Loo, and G. Roelkens, "Ge-on-Si and Ge-on-SOI thermo-optic phase shifters for the mid-infrared," Opt. Express 22, 28479–28488 (2014).